Selective Hg^{2+} sensor: rGO-blended PEDOT:PSS conducting polymer OFET

Published: 05 February 2021

Volume 127, article number 167, (2021) Cite this article

Applied Physics A

Aims and scope

Submit manuscript

Pasha W. Sayyad, Nikesh N. Ingle, Theeazen Al-Gahouari, Manasi M. Mahadik, Gajanan A. Bodkhe, Sumedh M. Shirsat & Mahendra D. Shirsat

Abstract

The detection of water pollutants employing organic field-effect transistor (OFET) sensor requires a stable performance in an aqueous media. It is an essential condition of any sensor to present reliable measurements. Some organic-conducting polymers deteriorate almost immediately in the presence of an aqueous medium. However, poly(3,4-ethylenedioxythiophene):poly(styrenesulfonate) (PEDOT:PSS) has proven its stability in both air and aqueous mediums. Nevertheless, due to inadequate structural and chemical properties of the PEDOT:PSS, it persists major obstacles and inhibits its performance in practical applications. These shortcomings can be overcome with the combination of carbon nanomaterials. Therefore, the present study deals with the effect of inclusion of

reduced graphene oxide (rGO) into PEDOT:PSS, and it resulted in the enhancement of structural, morphological, and electrical properties of the PEDOT:PSS/rGO nanocomposite. The organic field-effect transistor (OFET) was fabricated with PEDOT:PSS/rGO nanocomposite to detect heavy-metal ions. This makes a highly sensitive and selective sensor platform for detecting Hg^{2+} in the linear concentration range of 1–60 nM. The presented OFET sensor manifests high sensitivity and selectivity to Hg^{2+} with a low detection limit of 2.4 nM. The variety of metal ions tested, i.e., Hg^{2+}, Cd^{2+}, Pb^{2+}, Cu^{2+}, Zn^{2+}, Na^{+}, and Fe^{3+}, to investigate the selectivity. The sensor exhibits stable performance in an aqueous medium for the detection of Hg^{2+} in the presence of DI water. Moreover, the OFET sensor responded within 2–3 s after incubation of Hg^{2+} ions' solution.

1 Introduction

There is nothing more essential to human life for sustaining on earth than water, which presents a significant function in maintaining human health. Many people across the globe are struggling to have access to quality water for drinking. The industrial revolution has substantially increased due to Mercury exposure in drinking water. The increasing amount of mercury into the atmosphere, released from anthropogenic sources, results in human health risk. The increased exposure to mercury has adverse effects on the brain, heart, kidneys, lungs, immune system, and nervous system

[1,2,3,4,5,6,7]. Therefore, water pollution has become one of the significant issues globally, especially mercury, as a global pollutant. As direct exposure of heavy metals (mercury and other metal ions) leads to various health hazards, the control/detection of heavy-metal ions (HMIs) from aqueous media is of the initial concern and enormous importance of the present era. According to the guidelines of the United States Environmental Protection Agency (USEPA), the maximum acceptable concentration of Hg^{2+} in drinking water is 2 ppb (10 nM) [8].

The field-effect transistors (FETs) based on organic materials (OFETs) have started gaining researchers' attention. Large-scale fabrication, low-cost, portable, low-temperature, and biocompatible are a significant benefit of OFETs. Moreover, it exhibits high sensitivity and tunable property, which is made achievable through the simple solution and printing processability [9,10,11,12]. Recently, Minami et al. fabricated an extended gate (Au)-modified L-cysteine and dipicolylamine OFET sensor based on pBTTT-C_{16} as an active layer for the electrical detection of Hg^{2+} ions at 155 nM and 49.9 nM concentrations [13, 14]. Rullyani et al. reported the organic thin-film transistor (OTFT) for the detection of Hg^{2+} ions from aqueous medium using Pyrene-SH functionalization at the detection limit of 10 nM. However, it requires a high operating voltage [15]. Oren et al. have developed an OFET sensor based on DNA-functionalized Au NP/PII2T-Si for the detection of Hg^{2+} at 10 µM concentrations [16]. Nevertheless, the reported Hg^{2+} OFET sensors are less sensitive, require high operating voltage, and had detected at higher concentrations, which do not comply with the maximum acceptable concentration set by the EPA, USA. Moreover, the colorimetric, fluorometric, and electrochemical techniques also have been explored for Hg^{2+} detection. However, it could not achieve maximum contamination levels (MCL) recommended by the EPA, US [17,18,19,20]. Therefore, a sensor that overcomes the above obstacles is of conspicuous importance. It is advisable to build an analytical platform for the detection of heavy-metal ions from aqueous media.

Detection of HMIs in the presence of water requires stable polymeric materials for chemical sensor applications, and it is an inferable requirement of any sensor to produce reliable measurements. However, some polymeric materials (e.g., P3HT and PBTTT) are not stable in the water medium and degrade almost immediately [16, 21]. Their operational instability under aqueous medium has hindered the realization of their potential advantages. Therefore, alternative organic-conducting polymer material needs to be explored for the sensing application, which can be efficiently performed under liquid medium for the electrical detection of heavy-metal ions. Recently, the possible exploration of PEDOT:PSS in various applications such as solar cells, light-emitting diodes, and resistive switching devices have been explored [22,23,24]. The commercially available PEDOT:PSS has proven its stability in air and aqueous mediums [25, 26]. However, due to inadequate structural and chemical properties of the PEDOT:PSS, it persists major obstacles and inhibits its performance in practical applications. These shortcomings can be overcome with the combination of carbon nanomaterials [27]. Fascinating rGO

received much more attention because of its outstanding properties, i.e., high specific surface area, excellent electrical, mechanical, and biocompatible properties [28, 29]. Hence, it is a promising material to be explored for its possible inclusion into the PEDOT:PSS-conducting polymer matrix to enhance its electrical features [30]. The significant perspective of blending rGO into PEDOT:PSS is that (i) the PEDOT:PSS chains form over rGO sheets' surfaces through $\pi-\pi$ interactions between materials. (ii) It possesses the inherent property of electrical detection of chemical species due to high mobility [31,32,33,34]. By taking advantage of the outstanding properties of rGO, it is a convenient way to blend it into PEDOT:PSS, which can enhance the properties of host materials and will be suitable for the detection of heavy-metal ions from aqueous media.

Herein, we incorporated chemically reduced GO into commercially available PEDOT:PSS matrix, which resulted in the significant enhancement in the structural, morphological, and electrical conductivity. Further, the composite of PEDOT:PSS/rGO explored for heavy-metal ion detection. Moreover, the PEDOT:PSS/rGO nanocomposite can enhance the signal transduction at the electrolyte–electrode interface [29]. The presented OFET sensor manifests high sensitivity and selectivity to Hg^{2+} with a low detection limit of 2.4 nM. Moreover, the sensor exhibits stable performance in deionized (DI) water in the linear range of 1–60 nM.

2 Experimental

2.1 Chemicals

All the reagents required to synthesize graphene oxide (GO) are high purity grades (≥ 99%) and used without further purification. Graphite powder was procured from Merck, and phosphoric acid (H_3PO_4), sulfuric acid (H_2SO_4), hydrogen peroxide (H_2O_2), and potassium permanganate ($KMnO_4$) was procured from Sigma Aldrich. Hydrazine hydrate (N_2H_4) was purchased from Alfa Aesar and used without further purification. The commercially available poly(3,4-ethylene dioxythiophene) polystyrene sulfonate (PEDOT:PSS) was purchased from Sigma Aldrich, which has a concentration of 1.3 wt%. Heavy metal ion solution containing, i.e., Hg^{2+}, Cd^{2+}, Pb^{2+}, Cu^{2+}, Zn^{2+}, Fe^{3+}, and Na^{+}, was prepared by adding chloride salts in DI water.

2.2 Synthesis of graphene oxide (GO) and reduced graphene oxide (rGO)

Graphene oxide (GO) suspension was synthesized using the improved 'Hummers' method [35]. In short, the graphite powder (1 g) and $KMnO_4$ (6 g) were blended in one beaker and concentrated acidic solution of H_2SO_4/H_3PO_4 in a 9:1 volume ratio in another beaker. The solid mixture of graphite powder/KMnO4 slowly added in an acidic solution of H_2SO_4/H_3PO_4 in an ice bath at 5 °C temperature. The reaction was agitated for 12 h, accompanied by the addition of 10 mL of 30% H_2O_2 to terminate the

reaction. After that, the suspension was diluted with deionized water and centrifuged at 9000 rpm for 30 min to exclude the large aggregates and unreacted graphite. The GO was collected and purified by three times centrifugation. The obtained precipitate after centrifugation was GO and later explored for the reduction process. The chemical method was adopted to reduce GO using hydrazine hydrate. In brief, 50 mg of solid GO powder was dried at 50 °C for 24 h to synthesize rGO. Dried GO was dispersed in 50 ml of deionized water and ultrasonic treatment for 2 h to open the layers of GO. A 50 µl of hydrazine hydrate was introduced as a reducing agent into GO suspension and heated at 95 °C for 1 h and kept it in a hot oven to reduce graphene oxide (GO). After chemical reduction, the solution was centrifuged at 14,000 rpm for 30 min. The obtained precipitate was rGO.

2.3 Synthesis of PEDOT:PSS/rGO nanocomposite

The PEDOT:PSS/rGO composites were synthesized by the solution mixing method. The 5 ml solution of rGO was added to 5 ml of 1.3 wt% PEDOT:PSS aqueous dispersion solution at a volume ratio of 1:1, then stirred and ultrasonicated for 2 h at ambient temperature to get the homogeneous solution of PEDOT:PSS/rGO. Finally, the obtained PEDOT:PSS/rGO composite was subjected to electrical characterization and explored to develop the organic field-effect transistor (OFET) to detect heavy-metal ions.

2.4 Characterizations

Grazing incident X-ray diffraction pattern was recorded with Brucker (D8 Advance, Germany) at the power of 40 kV and 40 mA using Cu Kα radiation ($\lambda = 1.54059$ Å). Morphological characterization was carried out by atomic force microscopy (AFM) (Perk Systems, XE-7) and field emission scanning electron microscopy (FE-SEM) (Hitachi High-Technologies S4800) at 2 kV accelerating voltage. Raman scattering was recorded using XploRA PLUS Confocal Raman Microscope in the range of 200–3000 cm^{-1}. A maximum laser output power of 100 mW with a 785-nm laser diode was used as a wavelength source. Electrical characterizations and OFET-sensing experiments for detecting heavy-metal ions were recorded with Keithley 4200 SCS with probe station (Ecopia).

3 Results and discussion

3.1 X-ray diffraction

Grazing incident X-ray diffraction (GIXRD) pattern of GO, rGO, PEDOT:PSS, and PEDOT:PSS/rGO was studied to investigate the structural features, as shown in Fig. 1. Due to the amorphous nature of commercially available PEDOT:PSS polymer, no diffraction peaks were observed [36]. The GO diffraction peak at $2\theta = 9.74°$ reinforces the d-spacing of 0.90 nm, suggesting that the GO has

interlinked by hydroxyl and carboxyl functional groups, which manifest that the GO synthesized successfully. The GO peak at $2\theta = 9.74°$ disappear after the reduction process, and a broad diffraction peak at approximately $2\theta = 23.85°$ appeared due to the removal of oxygen-containing functional groups from GO. It indicates that rGO is synthesized successfully. The X-ray diffraction pattern for chemically reduced GO was well matched with previously reported data [37,38,39]. The average crystallite size and FWHM were calculated using DIFFRAC.EVA software. Debye–Scherrer's equation was applied to calculate an average crystallite size of rGO and PEDOT:PSS/rGO, as mentioned in the following equation [40,41,42,43,44,45,46,47,48,49]:

$$D = \frac{0.9\lambda }{{\beta \cos \theta }},$$

(1)

Fig. 1

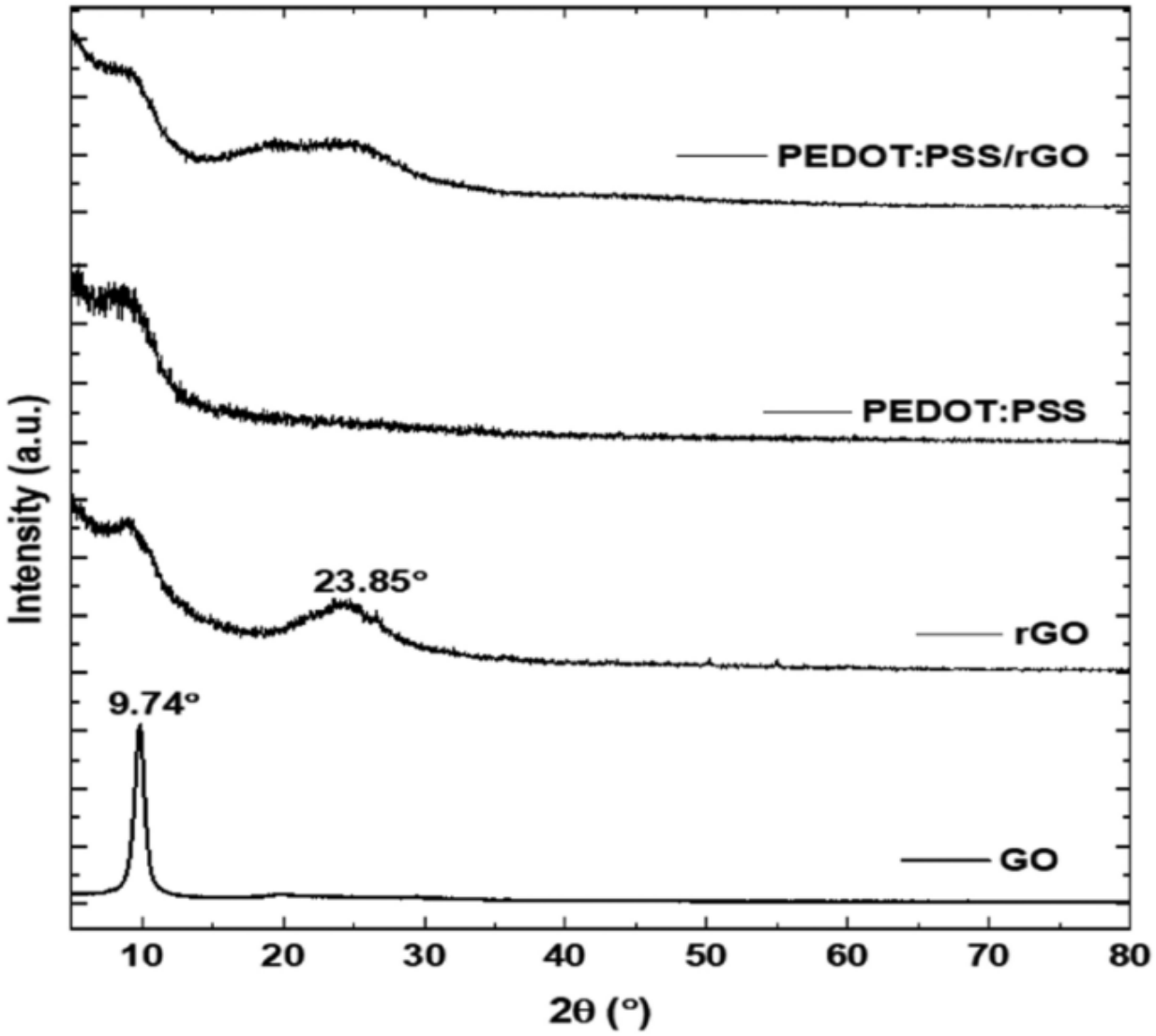

GIXRD pattern of GO, rGO, PEDOT:PSS and PEDOT:PSS/rGO nanocomposite

where D is an average crystallite size, \(\lambda\) is the X-ray copper tube wavelength, i.e., CuKα (1.5406 Å), \(\beta\) is full width at half maxima (FWHM), and θ is the Bragg angle. The average crystallite size of chemically reduced graphene oxide was 32.4 Å at FWHM 2.791. Whereas, the inclusion of rGO into PEDOT:PSS leads to an increase in average crystallite size of 49.3 Å at FWHM 1.830 for PEDOT:PSS/rGO. The increase in average crystallite size may contribute to carrier mobility enhancement [50], which will be suitable for detecting heavy metal ions sensitively.

3.2 Atomic force microscopy (AFM)

The morphological characterization was carried out at a scan rate of 0.5 Hz over a scan area of 3 µm × 3 µm. The surface properties were extracted using XEI AFM image processing and analysis software. A Gaussian function fitted to the AFM experimental data to calculate the average height of the GO, rGO, PEDOT:PSS, and PEDOT:PSS/rGO nanocomposite. AFM height histograms are depicted in Fig. 2a–d to reveal the surface area to volume ratio, average surface roughness, and surface height of synthesized materials and scanned micrographs displayed in the inset of Fig. 2a–d. The AFM micrograph of GO, shown in Fig. 2a, exhibits high surface area (9.62 μm^2), average surface roughness (18.80 nm), and average height (23.27 nm). The surface area, average surface roughness, and surface height of rGO decreased after the reduction of GO due to the removal of oxygen-containing functional groups from it, as shown in Fig. 2b. Due to uniform distribution and homogeneous surface area of PEDOT:PSS, it can be clearly seen in the inset of Fig. 2c, a 2D view, it exhibits low surface area, average surface roughness, and height. However, PEDOT:PSS/rGO nanocomposite exhibited higher surface area, average surface roughness, the height of 9.27 μm^2, 40.47 nm, and 7.91 ± 0.27 nm, suggesting the formation of PEDOT:PSS/rGO nanocomposite successfully. The surface area ratio, average surface roughness, and heights of the materials are shown in Table 1. The incorporation of rGO into PEDOT:PSS made a noticeable impact on enhancement in the surface area, average surface roughness, and height, as shown in Table 1. Moreover, the charge transport is more sensitive to the surface roughness of the sensing materials.

Fig. 2

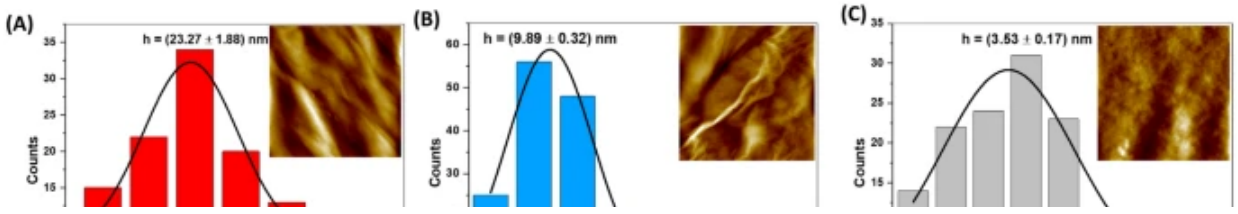

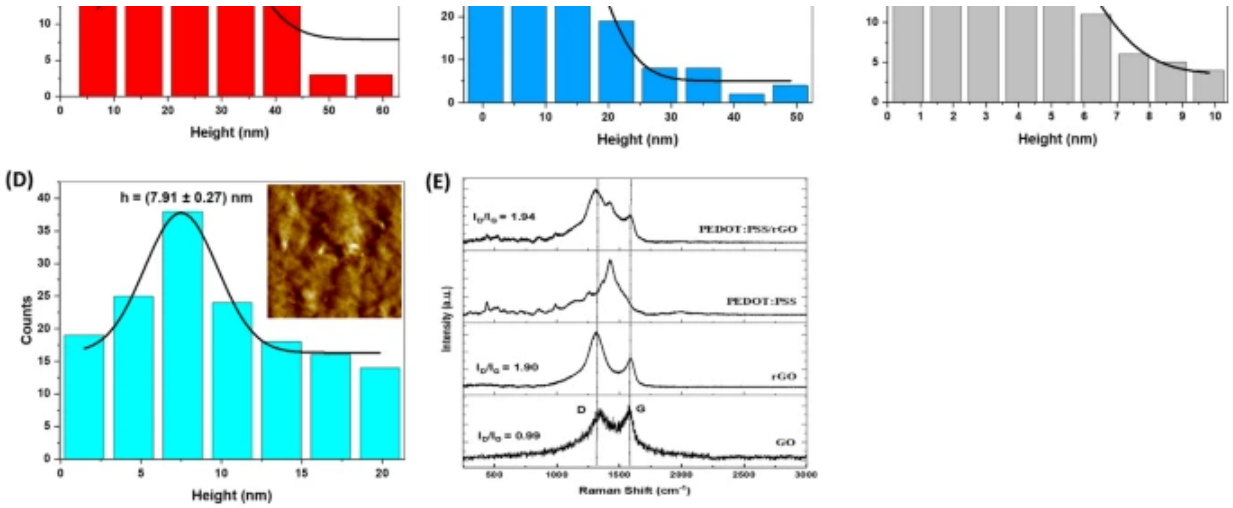

AFM surface height histograms (inset is the 2D view of AFM micrographs) of **a** GO, **b** rGO, **c** PEDOT:PSS, **d** PEDOT:PSS/rGO nanocomposite, and **e** Raman spectra

Table 1 Surface area, surface roughness, and average height of the materials

3.3 Raman spectroscopy

Raman spectra of GO, rGO, PEDOT:PSS, and PEDOT:PSS/rGO were recorded to examine structural disorder, as depicted in Fig. 2e. The Raman spectra of GO shown in Fig. 2e exhibited two prominent peaks: a D band and G band. The D band peak appeared at 1354 cm^{-1} associated with the sp^3 defects. Another G band peak at 1580 cm^{-1} attributed to the in-plane vibrations of sp^2 carbon atoms and a doubly degenerated phonon mode (E_{2g} symmetry) at the Brillouin zone center. The I_D/I_G ratio of GO exhibited 0.99, signifying that the smaller in-plane sp^2 domains have been created. The high-intensity D band in rGO and PEDOT:PSS/rGO compared to the G bands agreed with the expected graphitic defects of rGO. The oxygen functional groups have eliminated from an insulative GO due to the reduction process; it induces an improvement into the out-of-plane sp^2 vibrations of the carbon lattice and resulted in higher D band intensity in the Raman spectra of rGO and PEDOT:PSS/rGO [31]. The Raman spectra of PEDOT:PSS congruence well with previously reported data [51, 52]. The Raman peak for vibrational modes was observed at 1266 cm^{-1}, 1381 cm^{-1}, 1450 cm^{-1} attributed to the PEDOT group. The PSS vibrational modes are associated at around 1000 cm^{-1} and 1110 cm^{-1}. It has been implied that the thiophene-associated band of PEDOT:PSS reduces for the graphitic D and G bands in PEDOT:PSS/rGO. Since the PEDOT:PSS undergoes a structural transformation to promote the establishment of a unique $\pi-\pi$ interaction among PEDOT and the surface of the graphitic layers. Hence, in PEDOT:PSS/rGO

Raman spectra, PSS peaks diminished, and the PEDOT peak is visible. This implied that the rGO was successfully anchored over the PEDOT:PSS as evidence of an increase in the intensity ratio of D and G peak (1.94) in composite material, as depicted in Fig. 2e.

3.4 Field emission scanning electron microscopy (FESEM)

The surface morphology of the material is going to be very vital for sensor applications. Therefore, FESEM images of GO, rGO, PEDOT:PSS, and PEDOT:PSS/rGO were captured and shown in Fig. 3a–d. As shown in Fig. 3a, the occupancy of graphene layers is thinly crumpled, and wrinkled sheets were observed due to the oxidation of GO during the synthesis process. The few layers thick and few microns long rGO sheets, as shown in Fig. 3b, appeared to be less agglomerated, and individual sheets are easily recognizable as compared to GO (Fig. 3a), which demonstrates the successful reduction of graphene oxide. The FESEM image of PEDOT:PSS revealed the granular morphology, as demonstrated in Fig. 3c. However, the FESEM image of PEDOT:PSS/rGO appeared to be more agglomerated due to the re-formation of the $\pi-\pi$ stacking between PEDOT:PSS and rGO layers [53]. The incorporation of rGO into PEDOT:PSS shows that the interlayer separation of PEDOT:PSS appeared to be loaded with rGO. It can be inferred that the $\pi-\pi$ association has occurred between the layers of rGO and PEDOT:PSS [54], as shown in Fig. 3d. After that, several flaky agglomerated layers are found in the nanocomposites of PEDOT:PSS/rGO, which are also confirmed by AFM interpretation, as shown in Fig. 3d.

Fig. 3

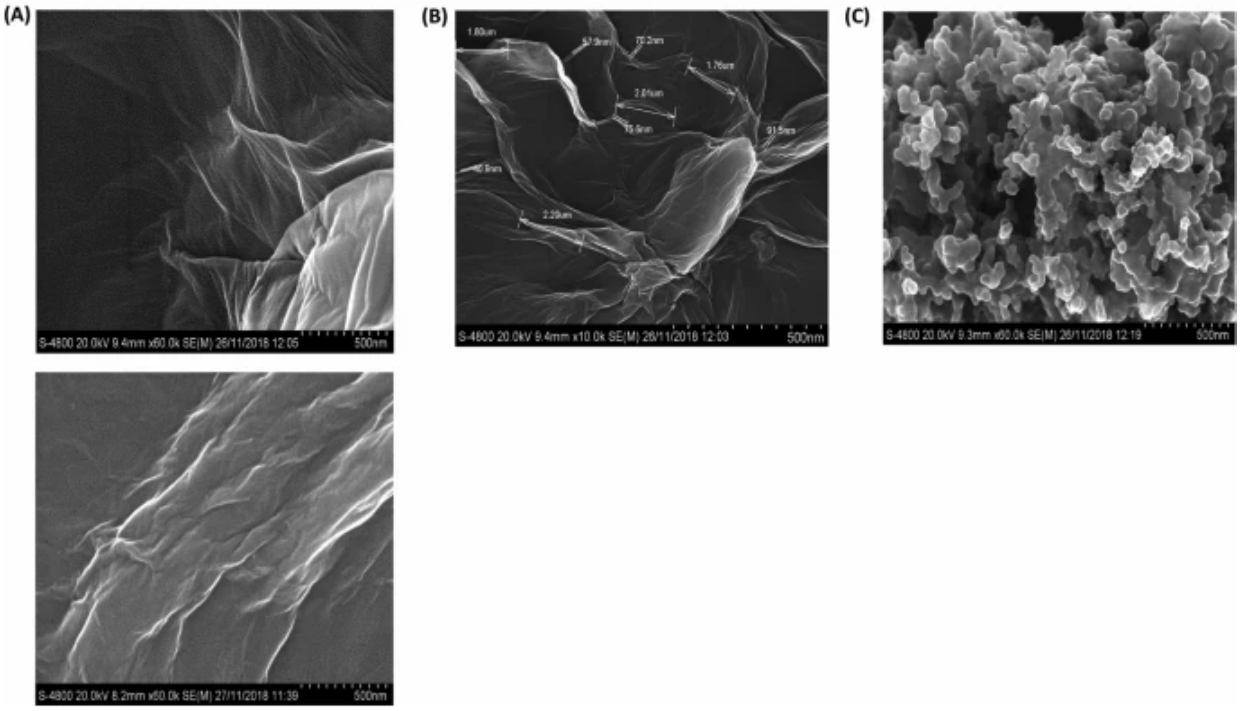

FE-SEM Images of **a** GO, **b** rGO, **c** PEDOT:PSS, and **d** PEDOT:PSS/rGO composite

3.5 Electrical characterization

The fabrication of the top contact bottom gated FET device was reported in our previous studies [55]. Before spin coat (3000 rpm for 60 s) composite of PEDOT:PSS/rGO over Si/SiO_2 substrate, it was washed with acetone followed by 2-propanol and dried using an N_2 flow gun and dehydrated at 120 °C. Gold (Au) microelectrode as source and drain (180 nm) coated via an e-beam using the thermal evaporation method. The target electrodes were developed on the Si/SiO_2 wafer using the lift-off method and used as a substrate for the OFET configuration. The bottom gate top contact OFET geometry was used on commercially available Si/SiO_2 substrate for the device transport characteristics, as shown in Fig. 4a. The formation of useful ohmic contacts confirmed by measuring the linear current–voltage (I–V) curve, as shown in Fig. 4b. The I–V characteristics of the PEDOT:PSS/rGO sensor exhibited the resistance value of 9.4 kΩ. The effect of blending rGO into PEDOT:PSS resulted in significant improvement in the conductivity, as depicted in Fig. 4b. The electrical characteristics, as shown in supporting information (Fig. S1), are the output and transfer characteristics curve of p-type PEDOT:PSS, which consists of a positively charged PEDOT chain and negatively charged PSS. The output and transfer characteristics of PEDOT:PSS/rGO are demonstrated in Fig. 4c, d. Gate potential was applied by varying V_{GS} from 0 to − 20 V with a step of - 5 V while measuring the output characteristics curve. The transfer characteristics curve (I_{DS} – V_{GS}) at constant V_{DS} = - 10 V was

measured with gate bias varying between the potential window − 40 to + 40 V for PEDOT:PSS and PEDOT:PSS/rGO nanocomposite.

Fig. 4

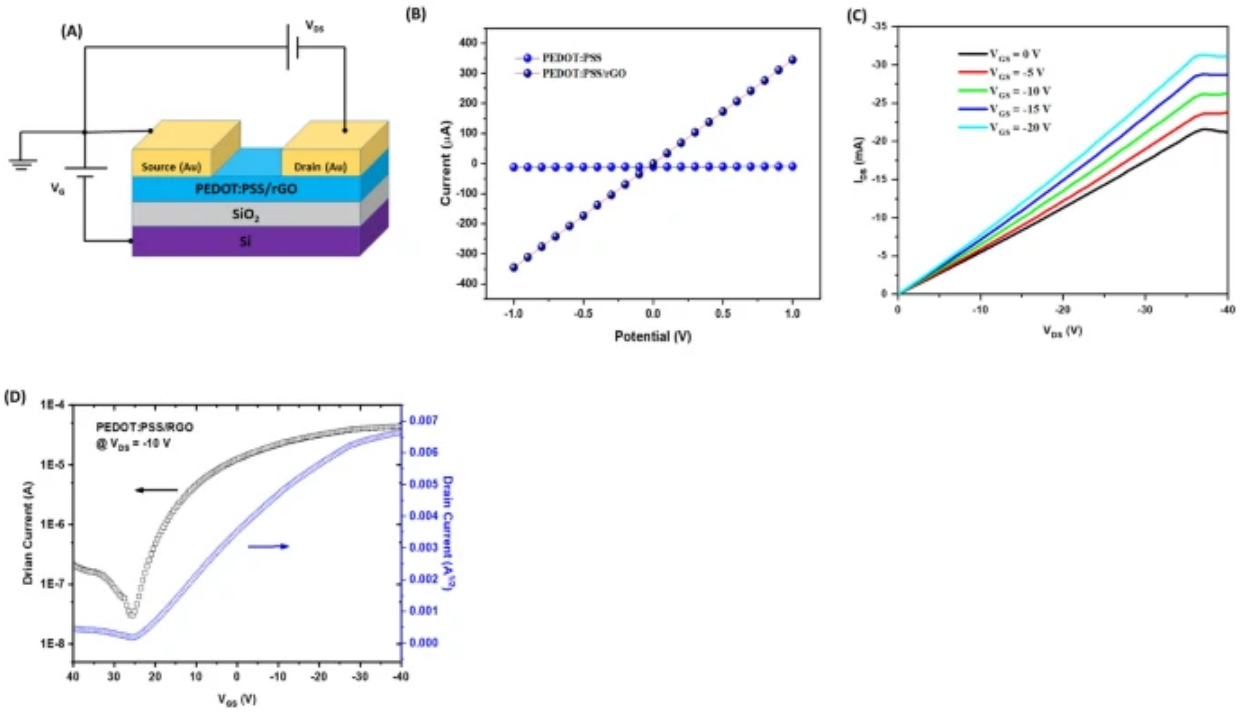

a Device architecture of an OFET, **b** *I*–*V* characteristics, **c** output, and **d** transfer characteristics of PEDOT:PSS/rGO nanocomposite. I_{DS} in transfer characteristics is plotted on a semi-logarithmic scale

The PEDOT:PSS exhibited carrier mobility of ~ 0.00549 $cm^2\ V^{-1}\ s^{-1}$, which is approximately comparable with the previous report [56]. The obtained threshold voltage is V_T = 33 V at V_{DS} = − 10 V with current on/off ratio 10^2. As compared to pristine PEDOT:PSS, the mobility in PEDOT:PSS/rGO relatively increases from ~ 0.00549 $cm^2\ V^{-1}\ s^{-1}$ to ~ 0.02 cm^2/Vs. The increase in mobility attributed to the rGO blending in PEDOT:PSS, which causes phase separation between PEDOT and PSS, enhances the PEDOT rich domains with longer conductive pathways leading to an increase in carrier mobility [57]. The fabricated PEDOT:PSS/rGO OFET device revealed excellent p-type behavior with average carrier mobility of ~ 0.02 cm^2/Vs at V_{DS} = − 10 V. The threshold voltage (V_T = 27 V) was extracted from the linear fit of $|I_{DS}|^{1/2}$ versus V_{GS} plots in the saturation regime. Moreover, the multilayers of graphene are a zero-overlap semimetal and contain both holes and electrons as charge carriers. The additional availability of the holes as a charge carrier in the PEDOT:PSS/rGO composite enhances the mobility. In addition, the increased average crystallite size and surface morphology also contributed to improved

mobility [58, 59], which are also supported by GIXRD and AFM interpretation. In OFET, the device current depends on mobility, and higher mobility materials have a higher current, which can be successfully employed to detect heavy metal ions. The carrier mobility was calculated using the transfer curve according to the following equation (see Table 2):

$$I_{{\text{D}}} = \left({ \frac{WCi}{{2L}} } \right) \mu (V_{{\text{G}}} - V_{{\text{T}}})^{2} ,$$

(2)

Table 2 The mobility and current on/off ratio of the materials

where I_D is the drain current, μ is the charge carrier mobility, C_i is the capacitance per unit area of the dielectric layer (SiO_2, 300 nm, Ci = 11 nF cm^{-2}). V_G signifies the gate voltage, V_T is the threshold voltage, W = 200 µm and L = 50 µm is the width and length of the channel, respectively. These results are in accordance with the earlier reported data [60,61,62]

3.6 Detection of heavy metal ions

All detection tests (sensing experiment) were conducted at room temperature. An organic field-effect transistor (OFET) architecture based on PEDOT:PSS/rGO channel was employed for these experiments, as presented in Fig. 5a. The channel conductivity was modulated by an Ag/AgCl reference electrode immersed in the electrolyte containing heavy metal ions by applying a voltage between the source and the drain electrode. OFETs exhibit a novel organic transistor configuration that facilitates low-voltage performance in water without a complex multi-layer pattern structure. The drain current (I_{DS}) was monitored during the cumulative incubation of the HMIs solution to the OFET sensor. OFET Sensing behavior of the final device (PEDOT:PSS/rGO) was tested to detect different heavy metal ions with concentrations ranging from 1 to 60 nM. The OFET sensor fabricated with PEDOT:PSS did not explore to heavy metal ion detection due to low electrical conductivity. The increase in electrical conductivity can be clearly seen after rGO blending, as depicted in Fig. 4b. The rGO material was utilized in the present investigation to enhance electrical conductivity in PEDOT:PSS-conducting polymer for OFET sensing of heavy metal ions.

Fig. 5

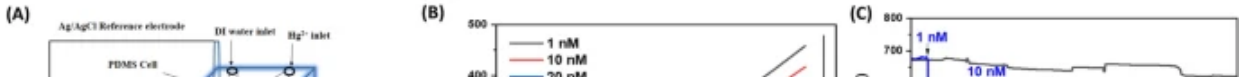

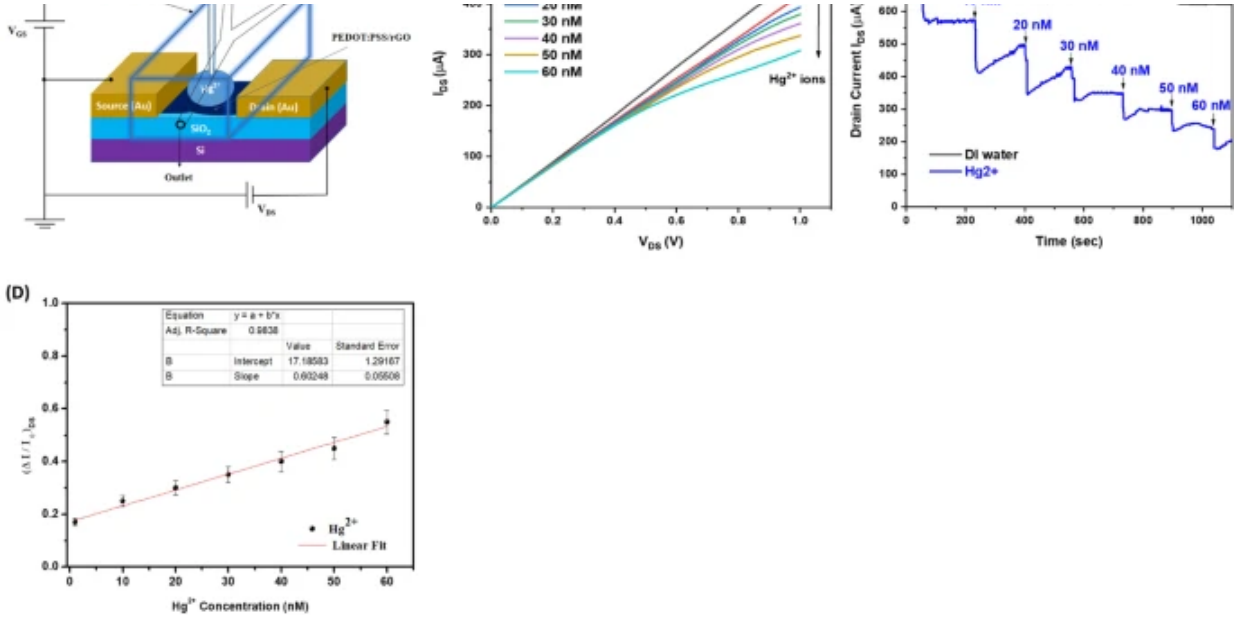

a Schematic structure of OFET sensor for HMI detection. **b** $I_{DS} - V_{DS}$ characteristics (at $V_{GS} = 0.2$ V) when sensor exposed to 1–60 nM of Hg^{2+} ion solutions. **c** Real-time detection ($V_{GS} = 0.2$ V & $V_{DS} = -0.1$ V) of Hg^{2+} in water. **d** Calibration curve of PEDOT:PSS/rGO for Hg^{2+} varying from 1 to 60 nM concentration

Then, the device was tested with common heavy metal ions including Hg^{2+}, Cd^{2+}, Pb^{2+}, Cu^{2+}, Zn^{2+}, Na^{+}, and Fe^{3+} to verify the selectivity. The strong response to Hg^{2+} ions was observed since it has a greater binding affinity to carbon allotropes than other heavy-metal ions. Our findings supported with the previous report for the heavy metal ion detection order $Hg^{2+} > > Cd^{2+} > Pb^{2+}$ are attributed to a carbon-based material [63]. Therefore, the output characteristics (I_{DS} vs. V_{DS}) of the OFET sensor for Hg^{2+} detection from 1–60 nM at $V_{GS} = 0.2$ reported in the present research work, as shown in Fig. 5b. The drain current of the PEDOT:PSS/rGO channel decreased significantly due to the diffusion of a liquid drop containing Hg^{2+} on the top of the channel, as shown in Fig. 5b. The sensor was tested at low gate voltage to avoid degradation due to doping and hydrolysis. The applied gate voltage should be well below 0.7 V to secure a stable device performance [64]. The decrease in drain current (I_{DS}) was observed as a function of the drain voltage ($V_{DS} = -0.1$ V) and the gate voltage ($V_{GS} = 0.2$ V) in response to Hg^{2+} ions exposure. The accumulation of Hg^{2+} causes to migrate the ions inside the grain boundaries and interrupting the flow of carrier concentration in the channel, resulting in a decrease in conductivity, as shown in Fig. 5c.

An OFET-sensing behavior based on drain current modulation was observed in response to a gradual increase in Hg^{2+} ions concentration by diluting the stock solution. The obtained detection limit in the

present investigation for Hg^{2+} sensor is comparatively low based on earlier reported organic-conducting polymer, as demonstrated in Table 3. The sensor performance was tested in the presence of DI water to examine the degradation of the sensor using the transfer characteristic curve on a linear scale, as shown in supporting information (Fig. S4). The sensor was stored in a vacuum desiccator and exposed immediately by a drop of DI water after taking samples from ambient to measure the transfer curve of PEDOT:PSS/rGO. The device maintained a good performance over a long time (30 days). The negligible shift in sensor performance was perceived due to the diffusion of water molecules.

Table 3 A comparison of the detection limit for the present Hg^{2+} OFET sensor with previously reported literature

The specificity of the (PEDOT:PSS/rGO) OFET sensor was investigated when it was exposed to solutions contain interfering ions such as Cd^{2+}, Pb^{2+}, Cu^{2+}, Zn^{2+}, Na^{+}, and Fe^{3+} ions, as shown in supporting information (Fig. S2). In the sensor characteristics, the most influential parameter is sensitivity. It is defined as the ratio of variation in current after adding ion ($\Delta I = I - I_0$) to the initial current (I_0). The highest sensitivity was obtained for Hg^{2+} ions compared with the other metal ions, as depicted in supporting information (Fig. S3). The obtained drain current response was in the following order Hg^{2+} > > Cd^{2+} > Pb^{2+} for PEDOT:PSS/rGO sensor, while Cu^{2+}, Zn^{2+}, Na^{+} and Fe^{3+} exhibited very weak response, as shown in supporting information (Fig. S2). The calibration curve of drain current response versus Hg^{2+} concentrations (1–60 nM) is shown in Fig. 5d. The obtained linear regression coefficient of 0.9838 was derived from the linear relationship between drain current responses versus Hg^{2+} concentrations. The 3σ method was applied to calculate the limit of detection (LOD), as mentioned in the following equation:

$$DL \, = \, 3\sigma /m,$$

(3)

where σ is the standard deviation, and m is the slope of the calibration line. Therefore, the obtained LOD of the sensor is 2.4 nM. Based on this measurement, the detection limit is 2.4 nM, as shown in Fig. 5c, but the sensor still exhibits a response to Hg^{2+} up to a 1 nM concentration. Selectivity histogram exhibiting responses to the various analyte (viz. Hg^{2+}, Cd^{2+}, Pb^{2+}, Cu^{2+}, Zn^{2+}, Na^{+}, and Fe^{3+}) is showed in supporting information (Fig. S3), it exhibits clear distinction of Hg^{2+} ions compared with other ions. The PEDOT:PSS/rGO OFET sensor reacted within few seconds after incubation of the Hg^{2+}

ions.

4 Conclusions

In summary, we have successfully incorporated rGO into PEDOT:PSS, which is resulted in the significant enhancement of structural, morphological, and electrical properties of the PEDOT:PSS/rGO nanocomposite. Then OFET sensor platform based on PEDOT:PSS/rGO was explored for Hg^{2+} ion sensing with a low detection limit of 2.4 nM. The selectivity of the sensor was verified by the exposure of various analyte (viz. Cd^{2+}, Pb^{2+}, Cu^{2+}, Zn^{2+}, Na^{+}, and Fe^{3+}). The sensor selectively responded to Hg^{2+} within 2–3 s after the exposure of ions solution. This sensor offers a good responsive route for selective, sensitive, high-performance, low-cost detection, user-friendly, and portable. Moreover, the sensor was stable in an aqueous medium containing metal ion solution. These results suggest an incredible potential for the commercialization of cutting-edge OFET sensor gadgets in various fields, such as smart health care, environmental monitoring for water purification, biomedical diagnostics, manufacturing, and military industries.

References

1. G.F. Nordberg, B.A. Fowler, M. Nordberg, *Handbook on the Toxicology of Metals* (Academic press, Cambridge, 2014).

Google Scholar

2. G. Genchi, M.S. Sinicropi, A. Carocci, G. Lauria, A. Catalano, Int. J. Environ. Res. Public Health **14**, 74 (2017)

Article Google Scholar

3. R. A. Bernhoft, J. Environ. Public Health **2012**, 1–31 (2012)

4. A. Sigel and H. Sigel, *Metal Ions in Biological Systems: Volume 32: Interactions of Metal Ions with Nucleotides: Nucleic Acids, and Their Constituents* (CRC Press, 1996)

5. K.M. Rice, E.M. Walker Jr., M. Wu, C. Gillette, E.R. Blough, J. Prev. Med. Public Health **47**, 74 (2014)

Article Google Scholar

6. J.-D. Park, W. Zheng, J. Prev. Med. Public Health **45**, 344 (2012)

Article Google Scholar

7. C.T. Driscoll, R.P. Mason, H.M. Chan, D.J. Jacob, N. Pirrone, Environ. Sci. Technol. **47**, 4967 (2013)

Article ADS Google Scholar

8. A. Spyropoulou, Y. G. Lazarou, and C. Laspidou, in *Multidisciplinary Digital Publishing Institute Proceedings* 2018, p. 668 (2018)

9. Y.H. Lee, M. Jang, M.Y. Lee, O.Y. Kweon, J.H. Oh, Chem **3**, 724 (2017)

Article Google Scholar

10. M. Watanabe, T. Miyazaki, T. Matsushima, J. Matsuda, C.-T. Chein, M. Shibahara, C. Adachi, S.-S. Sun, T.J. Chow, T. Ishihara, RSC Adv. **8**, 13259 (2018)

Article ADS Google Scholar

11. N. Ingle, P. Sayyad, G. Bodkhe, M. Mahadik, A.-G. Theeazen, S. Shirsat, M.D. Shirsat, Appl. Phys. A **126**, 1 (2020)

Article Google Scholar

12. N. Ingle, S. Mane, P. Sayyad, G. Bodkhe, T. Al-Gahouari, M. Mahadik, S. Shirsat, M.D. Shirsat, Front. Mater. **7**, 93 (2020)

Article ADS Google Scholar

13. T. Minami, T. Minamiki, S. Tokito, Jpn. J. Appl. Phys. **55**, 04EL02 (2016)

Article Google Scholar

14. T. Minami, Y. Sasaki, T. Minamiki, P. Koutnik, P. Anzenbacher, S. Tokito, Chem. Commun. **51**, 17666 (2015)

Article Google Scholar

15. C. Rullyani, M. Shellaiah, M. Ramesh, H.-C. Lin, C.-W. Chu, Org. Electron. **69**, 275 (2019)

Article Google Scholar

16. O. Knopfmacher, M.L. Hammock, A.L. Appleton, G. Schwartz, J. Mei, T. Lei, J. Pei, Z. Bao, Nat. Commun. **5**, 2954 (2014)

Article ADS Google Scholar

17. F. Tanvir, A. Yaqub, S. Tanvir, R. An, W.A. Anderson, Materials **12**, 1533 (2019)

Article ADS Google Scholar

18. S. Bayindir, J. Photochem. Photobiol. A **372**, 235 (2019)

Article Google Scholar

19. A. Moutcine, A. Chtaini, Sens. Bio-Sens. Res. **17**, 30 (2018)

Article Google Scholar

20. Kindly provide the complete details for the reference 21 (n.d.).

21. B. L. Rivas, B. F. Urbano, and J. Sánchez, Front. Chem. **6**, (2018).

22. H. Wen, H. Cai, Y. Du, X. Dai, Y. Sun, J. Ni, J. Li, D. Zhang, J. Zhang, Appl. Phys. A **123**, 14 (2017)

Article ADS Google Scholar

23. F. Hermerschmidt, F. Mathies, V.R. Schröder, C. Rehermann, N.Z. Morales, E.L. Unger, E.J. List-Kratochvil, Mater. Horizons **7**, 1773–1781 (2020)

Article Google Scholar

24. M.U. Khan, G. Hassan, M.A. Raza, J. Bae, Appl. Phys. A **124**, 726 (2018)

Article ADS Google Scholar

25. P.W. Sayyad, S.S. Khan, N.N. Ingle, G.A. Bodkhe, T. Al-Gahouari, M.M. Mahadik, S.M. Shirsat, M.D. Shirsat, Appl. Phys. A **126**, 1 (2020)

Article Google Scholar

26. P.W. Sayyad, N.N. Ingle, T. Al-Gahouari, M.M. Mahadik, G.A. Bodkhe, S.M. Shirsat, M.D. Shirsat, Chem. Phys. Lett. **761**, 138056 (2020)

Article Google Scholar

27. Y. Seekaew, S. Lokavee, D. Phokharatkul, A. Wisitsoraat, T. Kerdcharoen, C. Wongchoosuk, Org. Electron. **15**, 2971 (2014)

Article Google Scholar

28. T. Al-Gahouari, G. Bodkhe, P. Sayyad, N. Ingle, M. Mahadik, S.M. Shirsat, M. Deshmukh, N. Musahwar, M. Shirsat, Front. Mater. **7**, 68 (2020)

Article ADS Google Scholar

29. M. Mahadik, H. Patil, G. Bodkhe, N. Ingle, P. Sayyad, T. Al-Gahaouri, S. Shirsat, M.D. Shirsat, Front. Mater. **7**, 81 (2020)

Article ADS Google Scholar

30. M. Hakimi, A. Salehi, F.A. Boroumand, Fabrication and characterization of an ammonia gas sensor based on PEDOT-PSS with N-doped graphene quantum dots dopant. IEEE Sens. J. **16**, 6149–6154 (2016)

Article ADS Google Scholar

31. F. Abd-Wahab, A. Guthoos, H. Farhana, W. Salim, W.W. Amani, Biosensors **9**, 36 (2019)

Article Google Scholar

32. M. Zhang, W. Yuan, B. Yao, C. Li, G. Shi, ACS Appl. Mater. Interfaces. **6**, 3587 (2014)

Article Google Scholar

33. B.J. Kim, M.S. Kang, V.H. Pham, T.V. Cuong, E.J. Kim, J.S. Chung, S.H. Hur, J.H. Cho, J. Mater. Chem. **21**, 13068 (2011)

Article Google Scholar

34. C.W. Lee, J.M. Suh, H.W. Jang, Front. Chem. **7**, 708 (2019)

Article ADS Google Scholar

35. P. W. Sayyad, Z. A. Shaikh, N. N. Ingle, T. Al-Gahouari, M. M. Mahadik, G. A. Bodkhe, S. M. Shirsat, and M. D. Shirsat, in *Journal of Physics: Conference Series* (IOP Publishing, 2020), vol. 1644, p. 012001.

36. J. Li, J. Liu, C. Gao, J. Zhang, H. Sun, Int. J. Photoenergy **2009**, (2009).

37. I.A. Latif, S.H. Merza, Nanosci. Nanotech. **6**, 24 (2016)

Google Scholar

38. B. Rajagopalan, J.S. Chung, Nanosc. Res. Lett. **9**, 535 (2014)

Article Google Scholar

39. H. Saleem, M. Haneef, H.Y. Abbasi, Mater. Chem. Phys. **204**, 1 (2018)

Article Google Scholar

40. D. Dastan, Appl. Phys. A **123**, 699 (2017)

Article ADS Google Scholar

41. W.-D. Zhou, D. Dastan, J. Li, X.-T. Yin, Q. Wang, Nanomaterials **10**, 785 (2020)

Article Google Scholar

42. G.-L. Tan, D. Tang, D. Dastan, A. Jafari, J. P. Silva, X.-T. Yin, Mater. Sci. Semicond. Process. **122**, 105506 (2020)

43. P.W. Sayyad, N.N. Ingle, G.A. Bodkhe, M.A. Deshmukh, H.K. Patil, S.M. Shirsat, F. Singh, M.D. Shirsat, Radiat. Effects and Defects Solids **175**, 1 (2020)

Article Google Scholar

44. S.S. Kulkarni, G.A. Bodkhe, P.W. Sayyad, M.A. Deshmukh, S.S. Hussaini, M.D. Shirsat, International J. Nanosci. **19**, 2050009 (2020)

Article ADS Google Scholar

45. A. Jafari, K. Tahani, D. Dastan, S. Asgary, Z. Shi, X.-T. Yin, W.-D. Zhou, H. Garmestani, Ş Ţălu, Surf. Interfaces **18**, 100463 (2020)

Article Google Scholar

46. D. Dastan, N. Chaure, M. Kartha, J. Mater. Sci.: Mater. Electron. **28**, 7784 (2017)

Google Scholar

47. D. Dastan, S.L. Panahi, N.B. Chaure, J. Mater. Sci. Mater. Electron. **27**, 12291 (2016)

Article Google Scholar

48. D. Dastan, P.U. Londhe, N.B. Chaure, J. Mater. Sci. Mater. Electron. **25**, 3473 (2014)

Article Google Scholar

49. P. C. Yadav, M. A. Deshmukh, H. K. Patil, G. A. Bodkhe, P. W. Sayyad, N. N. Ingle, and M. D. Shirsat, in *AIP Conference Proceedings* (AIP Publishing LLC, 2018), p. 100058.

50. Kindly provide the complete details for the reference 51 (n.d.).

51. P.C. Mahakul, K. Sa, B. Das, B. Subramaniam, S. Saha, B. Moharana, J. Raiguru, S. Dash, J. Mukherjee, P. Mahanandia, J. Mater. Sci. **52**, 5696 (2017)

Article ADS Google Scholar

52. B. Xu, S.-A. Gopalan, A.-I. Gopalan, N. Muthuchamy, K.-P. Lee, J.-S. Lee, Y. Jiang, S.-W. Lee, S.-W. Kim, J.-S. Kim, Sci. Rep. **7**, 45079 (2017)

Article ADS Google Scholar

53. S. Deng, V. Berry, Mater. Today **19**, 197 (2016)

Article Google Scholar

54. D. Yoo, J. Kim, J.H. Kim, Nano Res. **7**, 717 (2014)

Article Google Scholar

55. G.A. Bodkhe, M.A. Deshmukh, H.K. Patil, S.M. Shirsat, V. Srihari, K.K. Pandey, G. Panchal, D.M.

Phase, A. Mulchandani, M.D. Shirsat, J. Phys. D Appl. Phys. **52**, 335105 (2019)

Article Google Scholar

56. S.A. Rutledge, A.S. Helmy, J. Appl. Phys. **114**, 133708 (2013)

Article ADS Google Scholar

57. A. Hasani, H. Sharifi Dehsari, M. Asghari Lafmejani, A. Salehi, F. Afshar Taromi, K. Asadi, Phys. Status Solidi (RRL) Rapid Res. Lett. **12**, 1870317 (2018)

Article ADS Google Scholar

58. N. Rolland, J.F. Franco-Gonzalez, R. Volpi, M. Linares, I.V. Zozoulenko, Phys. Rev. Mater. **2**, 045605 (2018)

Article Google Scholar

59. G. Horowitz, M.E. Hajlaoui, Synth. Met. **122**, 185 (2001)

Article Google Scholar

60. D. Dastan, A. Banpurkar, J. Mater. Sci. Mater. Electron. **28**, 3851 (2017)

Article Google Scholar

61. M. Fathinezhad, M. AbbasiTarighat, D. Dastan, Environmental Nanotechnology. Monit. Manag. **14**, 100307 (2020)

Google Scholar

62. D. Dastan, S.W. Gosavi, N.B. Chaure, Macromol. Symp. **347**, 81 (2015)

Article Google Scholar

63. I. Shtepliuk, N.M. Caffrey, T. Iakimov, V. Khranovskyy, I.A. Abrikosov, R. Yakimova, Sci Rep **7**, 3934 (2017)

Article ADS Google Scholar

64. K. Schmoltner, J. Kofler, A. Klug, E.J. List-Kratochvil, Adv. Mater. **25**, 6895 (2013)

Article Google Scholar

Acknowledgements

The authors extend their sincere thanks to DST-SERB, New Delhi (Project No. EEQ/2017/000645), Rashtriya Uchachatar Shiksha Abhiyan (RUSA), Government of Maharashtra, UGC—DAE CSR (RRCAT), Indore (Project No. CSR-IC-BL66/CRS- 183/2016-17/847), Inter University Accelerator Center (IUAC), New Delhi, India (UFR no. 62320), UGC-SAP Programme (F.530/16/DRS-I/2016 (SAP-II) Dt.16-04-2016) and DST-FIST (Project No. No. SR/FST/PSI-210/2016(C) dtd. 16/12/2016) for providing financial support.

Author information

Authors and Affiliations

RUSA Centre for Advanced Sensor Technology, Department of Physics, Dr. Babasaheb Ambedkar Marathwada University, Aurangabad, Maharashtra, India

Pasha W. Sayyad, Nikesh N. Ingle, Theeazen Al-Gahouari, Manasi M. Mahadik, Gajanan A. Bodkhe & Mahendra D. Shirsat

Department of Electronics and Telecommunication Engineering, Jawaharlal Nehru Engineering College, Aurangabad, Maharashtra, India

Sumedh M. Shirsat

Corresponding author

Correspondence to Mahendra D. Shirsat.

Additional information

Publisher's Note

Supplementary Information

Below is the link to the electronic supplementary material.

Supplementary file1 (DOCX 533 KB)

Rights and permissions

About this article

Cite this article

Sayyad, P.W., Ingle, N.N., Al-Gahouari, T. *et al.* Selective Hg^{2+} sensor: rGO-blended PEDOT:PSS conducting polymer OFET. *Appl. Phys. A* **127**, 167 (2021). https://doi.org/10.1007/s00339-021-04314-1

Received	Accepted	Published
27 September 2020	04 December 2020	05 February 2021

DOI
https://doi.org/10.1007/s00339-021-04314-1

Share this article

Keywords

Heavy-metal ions detection | Hg^{2+} detection | Organic field-effect transistor (OFET) | PEDOT:PSS | Reduced graphene oxide (rGO)